nature materials

Article

https://doi.org/10.1038/s41563-024-02079-5

Double-sided van der Waals epitaxy of topological insulators across an atomically thin membrane

Received: 30 May 2024

Accepted: 12 November 2024

Published online: 22 January 2025

Check for updates

Joon Young Park[1,2], Young Jae Shin[1], Jeacheol Shin[2], Jehyun Kim[2], Janghyun Jo[3], Hyobin Yoo[1,3,4], Danial Haei[1,5], Chohee Hyun[6], Jiyoung Yun[2], Robert M. Huber[7,8], Arijit Gupta[7,8], Kenji Watanabe[9], Takashi Taniguchi[10], Wan Kyu Park[8], Hyeon Suk Shin[11,12], Miyoung Kim[3], Dohun Kim[2], Gyu-Chul Yi[2] ✉ & Philip Kim[1] ✉

Atomically thin van der Waals (vdW) films provide a material platform for the epitaxial growth of quantum heterostructures. However, unlike the remote epitaxial growth of three-dimensional bulk crystals, the growth of two-dimensional material heterostructures across atomic layers has been limited due to the weak vdW interaction. Here we report the double-sided epitaxy of vdW layered materials through atomic membranes. We grow vdW topological insulators Sb_2Te_3 and Bi_2Se_3 by molecular-beam epitaxy on both surfaces of atomically thin graphene or hexagonal boron nitride, which serve as suspended two-dimensional vdW substrate layers. Both homo- and hetero-double-sided vdW topological insulator tunnel junctions are fabricated, with the atomically thin hexagonal boron nitride acting as a crystal-momentum-conserving tunnelling barrier with abrupt and epitaxial interfaces. By performing field-angle-dependent magneto-tunnelling spectroscopy on these devices, we reveal the energy–momentum–spin resonance of massless Dirac electrons tunnelling between helical Landau levels developed in the topological surface states at the interfaces.

Two-dimensional (2D) van der Waals (vdW) heterostructures composed of materials with various electronic properties serve as versatile platforms to explore a variety of interesting physical properties and device applications[1,2]. One of the most intriguing systems is a vertical heterostructure consisting of two materials separated by an atomically thin insulating barrier, allowing vertical tunnelling transport through vdW interfaces[3–5]. Such a heterostructure with high crystal quality and epitaxial alignment is of particular interest because crystal momentum parallel to the interface can be conserved, offering a unique platform for investigating the intrinsic selection rules of the resonant tunnelling process[6–8]. The surface states of three-dimensional (3D) vdW topological insulators (TIs) of $(Bi, Sb)_2(Te, Se)_3$ compounds[9], when integrated into vdW tunnel junctions, can provide exciting opportunities to discover interesting quantum phenomena occurring at the atomically sharp epitaxial interface between topologically dissimilar atomic layers[10–15].

Multilayer TI/normal insulator vdW heterostructures have been constructed by sequential direct growth using molecular-beam epitaxy (MBE)[10,16], a scalable approach that produces structurally aligned heterostructures with clean interfaces[2]. In this conventional MBE growth, however, the choice of barrier materials is limited by the need for chemical compatibility and lattice-constant matching. These constraints, in turn, restrict the tunnelling barrier height and the minimum distance between topological surface states (TSSs), which are critical parameters for tunnelling spectroscopy and coupling between TSSs. Furthermore, the common occurrence of step edges during the growth

A full list of affiliations appears at the end of the paper. ✉e-mail: gcyi@snu.ac.kr; pkim@physics.harvard.edu

https://doi.org/10.1038/s41563-024-02079-5

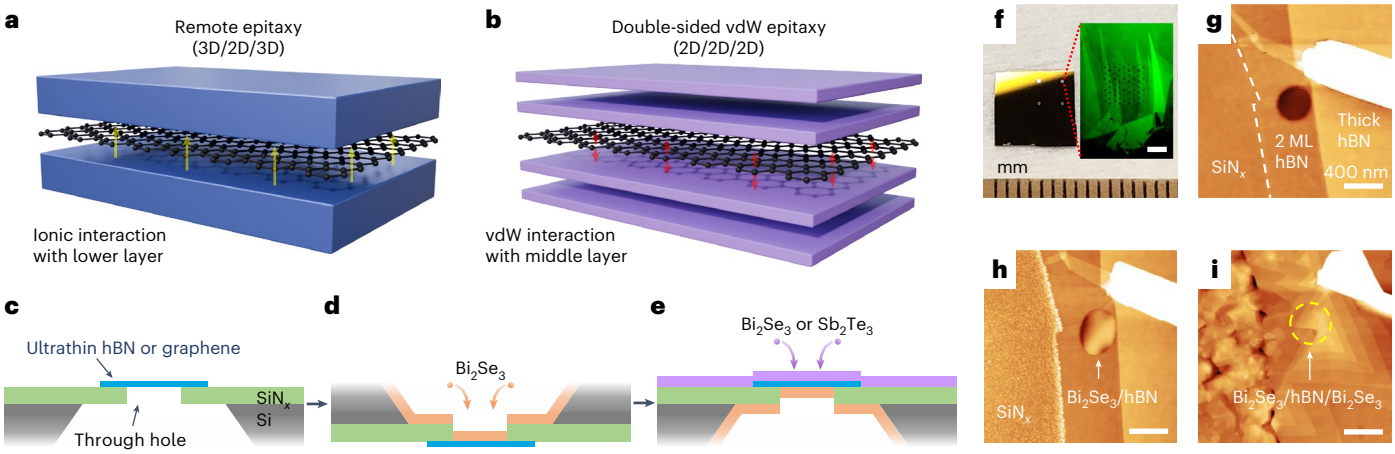

Fig. 1 | Double-sided vdW epitaxy of TI/hBN (graphene)/TI vertical heterostructures. a,**b**, Schematic illustrating the growth mechanism of remote epitaxy (**a**) and double-sided vdW epitaxy (**b**). In remote epitaxy, the middle 2D vdW layer serves as an atomically thin spacer to mediate the long-range interaction between 3D crystals. In the new concept of double-sided vdW epitaxy, the middle vdW layer serves as an atomically thin growth template, where the top and bottom layers are epitaxially connected by the short-range vdW interaction. **c**–**e**, Schematic of the double-sided vdW epitaxy procedure. An atomically thin hBN or monolayer graphene is suspended on a perforated SiN_x membrane (**c**). The chip is inverted and loaded into a UHV MBE chamber, where a Bi_2Se_3 thin film is grown on one side of the suspended vdW substrate (**d**). The chip is then flipped back, and a Bi_2Se_3 or Sb_2Te_3 thin film is grown on the other surface of the suspended vdW substrate (**e**). **f**, Photograph of an array of SiN_x membrane windows compatible with MBE, TEM and microfabrication. Inset: high-contrast optical microscopy image of an array of holes fabricated in the SiN_x membrane covered by an atomically thin hBN crystal. Scale bar, 10 µm. **g**–**i**, Atomic force microscopy topographic images (20 nm colour scale; taken from the front side) of 2 ML hBN suspended over one of the holes in the SiN_x membrane taken before (**g**) and after (**h**) the first growth of Bi_2Se_3 on the back side, and after the second growth of Bi_2Se_3 on the front side (**i**). Scale bars, 400 nm.

process substantially reduces the effectiveness of forming smooth vdW heterointerfaces.

The vdW epitaxy on both surfaces of an atomically thin, single-crystalline suspended vdW membrane opens a new way to construct TI epitaxial heterostructures with atomically sharp interfaces. The synthesis route presented in this work is distinguished from the recently demonstrated remote epitaxy of 3D/2D/3D hybrid systems. In remote epitaxial growth, the electrostatic field of the substrate (lower 3D layer) penetrates the 2D vdW interlayer (Fig. 1a)[17,18]. Due to its strong dependence on the ionic character or polarity of the 3D substrate, remote epitaxy establishes the long-range epitaxial relationship between 3D/3D bulks, insensitive to the crystallographic alignment at the 3D/2D local interfaces. On the contrary, in the newly proposed double-sided vdW epitaxy (Fig. 1b), one can utilize the short-range local vdW interaction at the interfaces, structurally connecting the top and bottom epilayers to the substrate (middle) layer. Moreover, unlike remote epitaxy in which a stronger coupling leads to a stronger correlation of the electronic structure across the heterostructure, the electrical coupling can be tuned independently by the thickness and electronic properties of the middle layer. So far, although 3D/2D/3D quasi-vdW epitaxial double heterostructures have been demonstrated in the form of graphene sandwiched by semiconductor nanostructures with reconstructed dangling bonds of polar facets at the interface[19,20], all-2D double-sided vdW epitaxy has not yet been realized. In this Article, we present the double-sided vdW MBE growth of 2D/2D/2D structures in which two epitaxially aligned TIs are separated by atomically thin crystalline barriers with abrupt interfaces, which has enabled us to observe the resonant tunnelling between Landau levels (LLs) developed in the TSSs at the vdW heterointerface at which the energy, momentum and spin of the helical Dirac fermions are conserved during the tunnelling process.

The method developed to fabricate the double-sided epitaxial vdW heterostructures is schematically illustrated in Fig. 1c–e. Ultrathin hexagonal boron nitride (hBN) layers (2–5 monolayers; MLs) or monolayer graphene is suspended over hole arrays pre-patterned in SiN_x membranes to expose both surfaces (Fig. 1f and Extended Data Fig. 1). Subsequently, Bi_2Se_3 (n-type) and Sb_2Te_3 (p-type) thin films are heteroepitaxially grown on each side of the suspended layer using ultrahigh-vacuum (UHV) MBE (Methods and Extended Data Fig. 2). The suspended vdW layer serves as a crystalline substrate for the epitaxy of TI films. In particular, the atomically thin hBN layers can serve as a wide-bandgap insulating barrier for tunnelling spectroscopy between the two TIs whose interface is sealed under UHV. Since the suspended vdW heterostructures are electron transmitting and mechanically robust, this templated growth approach enables us to directly use plan-view transmission electron microscopy (TEM) and atomic force microscopy to study their structural properties (Figs. 1g–i and 2) and the microfabrication processes to form electrical contacts to the junctions[21–24].

The microstructural properties of the TI/hBN (graphene)/TI heterostructures can be investigated by TEM. We first demonstrate that the bottom (b-Bi_2Se_3) and top (t-Bi_2Se_3) Bi_2Se_3 films are epitaxially aligned through a suspended monolayer graphene and a single-atom-thick vdW crystal substrate. Figure 2a shows the plan-view selected area electron diffraction (SAED) image of the resulting heterostructure exhibiting the preferential epitaxial relationship of $\{10\bar{1}0\}_{\text{b-Bi}_2\text{Se}_3} \parallel \{10\bar{1}0\}_{\text{graphene}} \parallel \{10\bar{1}0\}_{\text{t-Bi}_2\text{Se}_3}$. The weak Bragg peaks from Bi_2Se_3 with small deviation angles can be attributed to the wrinkles formed in the suspended vdW layers (Fig. 2a (inset) and ref. 23) and to grains with a small in-plane misorientation angle, which is probably due to the weak vdW interactions at the interface[22,25–27].

The same methodology can be applied to insulating hBN substrates, which is of particular interest for vertical tunnel junctions. The cross-sectional high-resolution (HR) TEM image (Fig. 2b) shows the quintuple-layer (QL) structures of the Bi_2Se_3 thin films, and the atomically clean and abrupt interfaces between b-Bi_2Se_3, 2 ML hBN and t-Bi_2Se_3 (Extended Data Fig. 3). As shown in Fig. 2, their epitaxial relationship can be confirmed by comparing the fast Fourier transform (FFT) of the representative areas (yellow and orange boxes) with the interfacial region (red box), where one can find matching structures of b- and t-Bi_2Se_3 (white arrows) relative to the hBN atomic registry (red arrow).

Next, we present the growth of dissimilar TI materials, namely, Bi_2Se_3 and Sb_2Te_3, across a suspended hBN, further demonstrating the power of our double-sided vdW epitaxy. Figure 2c shows the plan-view HR-TEM image of the Sb_2Te_3/hBN/Bi_2Se_3 heterostructure, taken near

https://doi.org/10.1038/s41563-024-02079-5

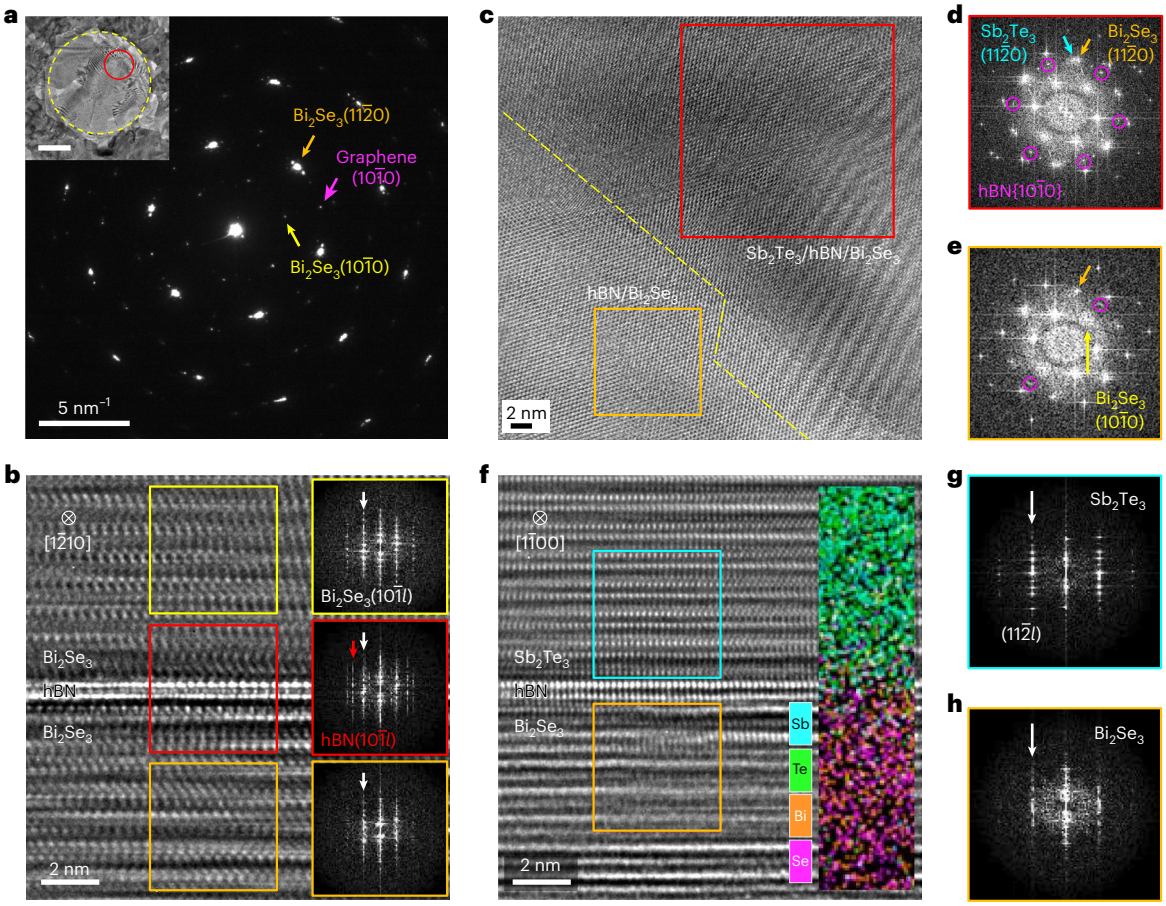

Fig. 2 | Structural properties of TI/hBN (graphene)/TI double-sided vdW epitaxial heterostructures. a, Plan-view SAED pattern of Bi_2Se_3/monolayer graphene/Bi_2Se_3. Inset: plan-view bright-field TEM image of the heterostructure. The dashed yellow circle and the red circle indicate the suspended area (a hole in the SiN_x membrane) and the area in which the SAED is recorded, respectively. Scale bar, 200 nm. **b**, Cross-sectional HR-TEM image of Bi_2Se_3/2 ML hBN/Bi_2Se_3 taken along the zone axis [1$\bar{2}$10]. Insets: FFT patterns of the areas corresponding to the yellow, red and orange boxes in the main panel. **c**, Plan-view HR-TEM image of Sb_2Te_3/few-layer hBN/Bi_2Se_3 taken around the boundary of Sb_2Te_3 (dashed yellow line). **d**,**e**, FFTs of the regions marked by the red (**d**) and orange (**e**) boxes in **c**. **f**, Cross-sectional HR-TEM image of Bi_2Se_3/2 ML hBN/Sb_2Te_3 taken along the zone axis [1$\bar{1}$00]. Inset: cross-sectional scanning TEM-energy-dispersive X-ray spectroscopy elemental mapping image. **g**,**h**, FFTs of the regions marked by the cyan (**g**) and orange (**h**) boxes in **f**.

the edge of a hole in the SiN_x membrane. Therefore, there is a region in which only Bi_2Se_3 is grown on hBN (first growth on the top side) without the coverage of Sb_2Te_3 (second growth on the bottom side). Although the moiré patterns arise from the lattice mismatch between Sb_2Te_3 and Bi_2Se_3 (~2.8%) (refs. 28,29) and their small in-plane misorientations (Fig. 2d), the FFT patterns of the selected areas of the image (Fig. 2d,e) identify the epitaxial alignment between Bi_2Se_3 and hBN as well as the epitaxial alignment between the Bi_2Se_3 and Sb_2Te_3 films through the hBN substrate: $\{10\bar{1}0\}_{Bi_2Se_3} \parallel \{10\bar{1}0\}_{hBN} \parallel \{10\bar{1}0\}_{Sb_2Te_3}$. The epitaxial relationship in our bidirectional MBE on suspended hBN and graphene is consistent with that of the TI thin films grown on a single surface of hBN and graphene substrates (Extended Data Fig. 4 and refs. 22,27), suggesting that the epitaxial alignment is mainly due to the interaction with the suspended vdW substrate layer.

The high interfacial quality of the heterostructure is also confirmed by the cross-sectional HR-TEM image (Fig. 2f). Since the strong and dense in-plane chemical bonding in the hBN layers provides a completely impermeable atomic membrane, we do not expect any interdiffusion of atoms through the hBN substrate during the growth of the second layer on the opposite side of the surface after the first-layer growth. Figure 2f (inset) shows the cross-sectional chemical composition analysis using scanning TEM equipped with energy-dispersive X-ray spectroscopy, demonstrating the clear spatial separation of Sb_2Te_3 and Bi_2Se_3 across the two-atom-thick hBN barrier. The epitaxial relationship across the hBN substrate can be reconfirmed by comparing the FFT patterns of Bi_2Se_3 and Sb_2Te_3. As shown in Fig. 2g,h, the (11$\bar{2}l$) spots of Bi_2Se_3 (Fig. 2g, white arrow) align well with the corresponding spots of Sb_2Te_3 (Fig. 2h, white arrow).

With the hBN barrier layer, our double-sided vdW epitaxy provides TI/hBN/TI tunnelling devices, enabling the study of the electron-tunnelling properties of helical Dirac fermions through the tunnelling barrier. To perform tunnelling spectroscopy, individual electrical contacts to an array of suspended junctions are fabricated on the top side, whereas they share a common bottom contact (Fig. 3a, Extended Data Fig. 5 and Methods). A d.c. bias voltage V is applied to the top electrode with respect to the bottom electrode, and the tunnelling current I can be measured across the junction. Although we have fabricated tunnelling devices on Bi_2Se_3/hBN/Bi_2Se_3 as well (the results are shown in Extended Data Fig. 6), in the remainder of this paper, we focus on the Bi_2Se_3 (bottom)/hBN/Sb_2Te_3 (top) heterostructure, whose configuration yields n-TI/insulator/p-TI junctions.

The Bi_2Se_3/hBN/Sb_2Te_3 heterojunction at zero bias is expected to form a type-III band alignment with a broken gap due to the large difference in their electron affinities and relatively small bulk bandgaps (Fig. 3b)[30,31]. Accordingly, charge transfer and band bending result in carrier accumulation near the junction. Away from the heterointerface, the Fermi level E_F of Bi_2Se_3 (Sb_2Te_3) films is located near the edge of the bulk conduction (valence) band due to the unintentional n-type

https://doi.org/10.1038/s41563-024-02079-5

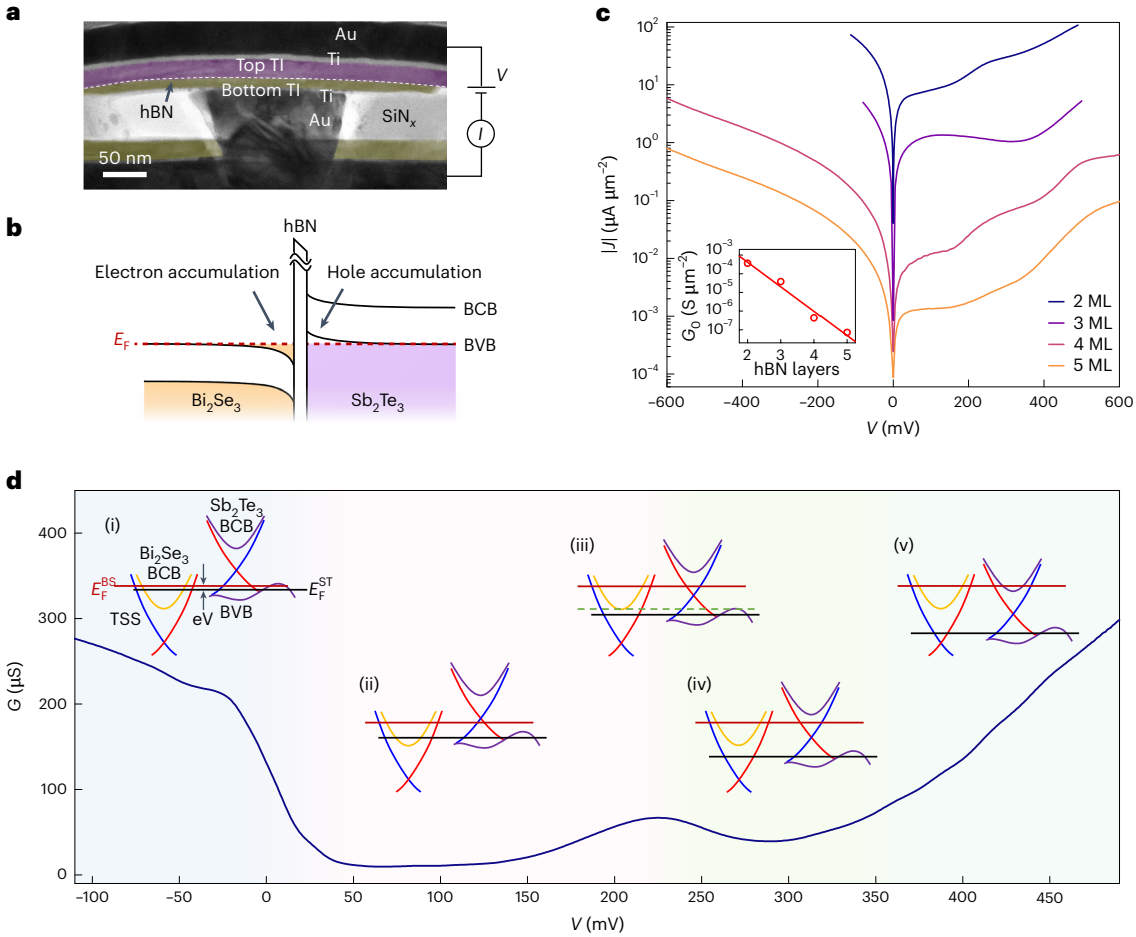

Fig. 3 | Tunnelling spectroscopy of Bi_2Se_3/hBN/Sb_2Te_3 junctions at zero magnetic field. a, False-coloured low-magnification cross-sectional bright-field TEM image of a vertical tunnel junction device in the two-terminal measurement configuration. Although this image shows Bi_2Se_3/hBN/Bi_2Se_3, the device structure is identical for all the measured junctions, including Bi_2Se_3/hBN/Sb_2Te_3, except for the hBN barrier thickness and the junction area. **b**, Schematic of the band alignment of the Bi_2Se_3/hBN/Sb_2Te_3 junction at zero bias voltage, depicted in the energy–out-of-plane axis plane. **c**, Tunnelling current density as a function of bias voltage for the devices with different thicknesses of hBN barrier. V is applied to Sb_2Te_3 (top), and the current that drains through Bi_2Se_3 (bottom), I, is measured. Inset: zero-bias differential conductance per unit area as a function of the number of hBN layers. The red line indicates an exponential fit. **d**, Differential conductance of the Bi_2Se_3/2 ML hBN/Sb_2Te_3 device as a function of V. (i)–(v) show the following. Schematic of the band alignments at the tunnelling interface under different bias conditions, plotted in the energy–in-plane momentum plane. TSSs are marked by red and blue colours, indicating their spin–momentum locking textures. The tunnelling conductance is determined by the positions of BCB and BVB relative to E_F^{BS} and E_F^{ST}. Devices with 2 ML and 3 ML hBN barriers are measured at $T = 1.8$ K and those with 4 ML and 5 ML barriers are measured at $T = 1.5$ K.

(p-type) doping[22,31,32]. The TSSs at the interface are, hence, electrically contacted by the bulk states. Since the grown TI films are thicker than 4 nm, the surface states of the individual TI slabs are not considerably hybridized[33,34], and the tunnelling resistance across the hBN separation layers is dominant in this measurement.

Figure 3c shows J–V, the current density J as a function of the applied bias voltage V, measured in devices with different hBN barriers ranging from 2 ML to 5 ML. For a negative bias voltage, $|J(V)|$ monotonically increases rapidly with increasing $|V|$. However, for positive bias, $J(V)$ increases non-monotonically as V increases, exhibiting negative-differential-conductance-like characteristics at a certain range of bias voltages, resulting in a lower current compared with negative bias. These features, together with the temperature dependence of the negative differential conductance behaviour (Extended Data Fig. 7), strongly support the fact that our tunnel diodes are formed by p–n junctions with broken-gap band alignments[35]. The measured differential conductance at zero bias, normalized by the nominal junction area, $G_0 = \partial J/\partial V$ ($V = 0$), scales exponentially with the thickness of the insulating hBN barrier (Fig. 3c, inset), suggesting that electron transport in our devices is dominated by tunnelling through the hBN barriers[36,37]. The tunnelling barrier height ϕ, estimated using the Wentzel–Kramers–Brillouin approximation $G_0 \propto \exp(-2t\sqrt{2m^*\phi}/\hbar)$, corresponds to $\phi \approx 3.0$ eV, assuming $m^* = 0.26m_e$ (ref. 37), where t is the thickness of hBN, m^* is the effective mass for the conduction band edge of hBN, m_e is the electron mass and $\hbar$ is the reduced Planck constant. This large barrier height allows us to investigate the tunnelling transport properties over a wide range of V as well as to bring two TSSs into close proximity.

The detailed tunnelling process in the junction can be described in the differential conductance $G(V) = \partial I/\partial V$ curve for the device with a 2 ML hBN barrier (Fig. 3d). Schematic of the band alignments at the heterointerface under different bias voltages are illustrated together, as labelled by (i)–(v) in Fig. 3d. The differential conductance exhibits a strongly reduced value between bias-voltage regions of (i) and (v), indicating that the Fermi level of n-Bi_2Se_3 (E_F^{BS}) crosses the bulk bandgap of p-Sb_2Te_3 as V increases in this region. As the Fermi level of p-Sb_2Te_3 (E_F^{ST}) moves out of the bulk conduction band (BCB) of n-Bi_2Se_3 and into its bulk bandgap ((ii) and (iv)), the $G(V)$ exhibits a peak at $V = 225$ mV (iii). This local maximum can be attributed to the enhanced tunnelling density of states due to the alignment between the Van Hove singularities[38,39] at the top of the M-shaped bulk valence band (BVB) of

https://doi.org/10.1038/s41563-024-02079-5

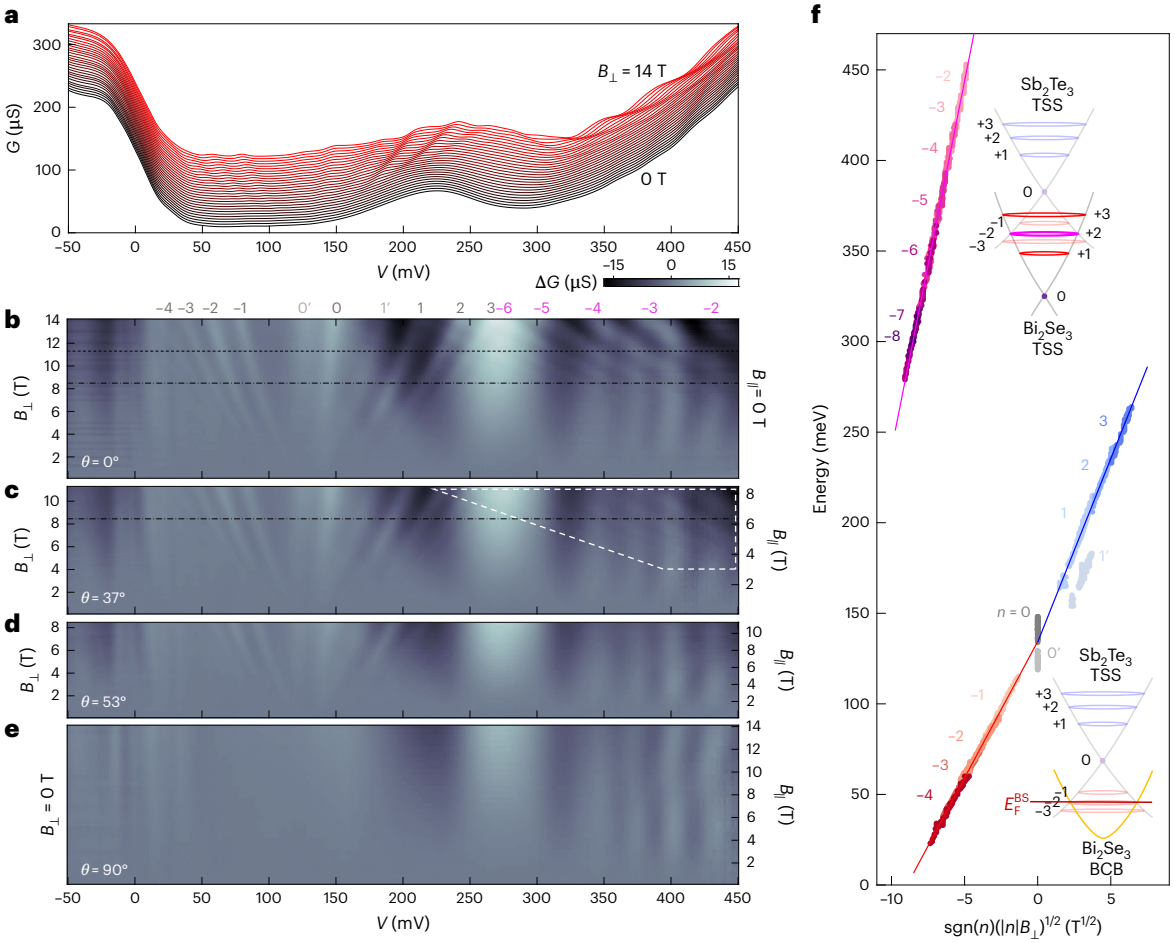

Fig. 4 | Magnetic-field-dependent tunnelling conductance of the Bi_2Se_3/2 ML hBN/Sb_2Te_3 device. a, $B_\perp$ dependence of tunnelling conductance. Spectra under different fields, in 0.5 T increments, are vertically offset by 4 μS for clarity. **b**–**e**, Colour-scale maps showing the field-modulated component of the conductance $\Delta G(V, B)$ at different field angles θ defined with respect to the out-of-plane direction. Perpendicular and in-plane components of the field are indicated by the left and right ticks, respectively. Vertical axes of **b**–**d** are adjusted to have the same $B_\perp$ scale, whereas those of **b** and **e** have the same $|B|$ scale. The black dashed (dash–dotted) horizontal line indicates the maximum $B_\perp$ value in **c** (**d**). **f**, LL peak positions at different $B_\perp$ values plotted versus $\mathrm{sgn}(n)(|n|B_\perp)^{1/2}$. The lines are linear fits to the data. The bottom (top) inset is the schematic of the band alignment that causes the LL peaks in the tunnelling conductance to appear at lower (higher) bias voltages. The spin helicity of the TSSs is expressed in red and blue colours. Numbers denote the LL indices. All the measurements are performed at $T = 1.8$ K.

Sb_2Te_3 and the bottom of the BCB of Bi_2Se_3 with a substantial Rashba spin splitting, induced by interfacial band bending[40]. At $V \lesssim 40$ mV and $V \gtrsim 350$ mV, oscillatory spectral features appear due to the bulk quantum well states (QWSs) resulting from either the finite thickness of TI thin films[33,34] or band bending at the tunnelling interface[40].

The topological nature of the coupled surface states in our vdW epitaxial structure can be revealed by the magneto-tunnelling transport study. When a magnetic field perpendicular to the junction, $B_\perp$, is applied, LLs form in the TSSs, which can modulate the tunnel conductance associated with the TSSs[34,41–43]. Figure 4a shows the differential conductance spectra $G(V, B_\perp) = \partial I/\partial V(V, B_\perp)$ of the Sb_2Te_3/2 ML hBN/Bi_2Se_3 device at different $B_\perp$ values. As $B_\perp$ increases, the tunnelling conductance spectrum exhibits additional oscillatory features. A more systematic analysis can be performed by subtracting the zero-magnetic-field conductance: $\Delta G(V, B_\perp) = \partial I/\partial V(V, B_\perp) - \partial I/\partial V(V, B_\perp = 0)$. Figure 4b shows ΔG as a function of V and $B_\perp$. We observe that $\Delta G(V)$ oscillations exhibit larger amplitudes at higher $B_\perp$. These oscillatory features can be categorized into three groups: oscillations with peak and valley positions (1) that are independent of $B_\perp$; (2) that vary with $B_\perp$ and converge to $V \approx 135$ mV as $B_\perp$ vanishes; and (3) that vary with $B_\perp$ and converge to a large bias voltage ($V > 450$ mV) as we extrapolate the position of the origin.

To further investigate the nature of ΔG oscillation, we tilt the magnetic field B and provide a component of the magnetic field parallel to the junction, $B_\parallel$. Figure 4b–e shows $\Delta G(V, B)$ at different $B_\perp$ and $B_\parallel$ values. We find that the oscillatory feature (1) depends only on the total magnetic field B, indicating a 3D isotropic nature, whereas features (2) and (3) depend only on $B_\perp$, suggesting a 2D origin. We attribute feature (1) to bulk QWSs due to its angle insensitivity and the bias-voltage ranges in which the peaks appear (Extended Data Fig. 8 shows the field dependence of the bulk-originated peaks in G).

The 2D oscillatory features (2) and (3) can be related to resonant tunnelling associated with LL formation in the TSSs. In particular, the observed unequal spacing, which increases with increasing $B_\perp$, suggests that these LLs originate from the linearly dispersed Dirac spectrum of the TSSs. In a perpendicular magnetic field, the Dirac dispersion of the TSSs can lead to sharply quantized LLs at energy $E_n = E_D + \mathrm{sgn}(n)v_F\sqrt{2e\hbar|n|B_\perp}$, where E_D is the energy of the Dirac point, v_F is the Fermi velocity of the TSSs, e is the elementary charge and $n = 0, \pm1, \pm2\ldots$ is the LL index, ignoring the Zeeman energy[34,41–43]. As the bias voltage increases, $V > 20$ mV, resonant tunnelling between the BCB of Bi_2Se_3 and the LLs developed in the TSS of Sb_2Te_3 becomes possible. Indeed, the oscillatory feature (2) in the magneto-tunnelling spectra (Fig. 4b–d) follows $e(V - V_0) = \mathrm{sgn}(n)v_F\sqrt{2e\hbar|n|B_\perp}$, centred at

around $V_0 \approx 135$ mV. We identify the peaks of these oscillations, V_n, and assign the LL indices n as shown in Fig. 4b (top), marked by the grey font (Extended Data Fig. 9). We then plot the positions of the peaks in energy eV_n against $\mathrm{sgn}(n)\sqrt{|n|B_\perp}$ (Fig. 4f, bottom). Remarkably, all the data points for $n > 0$ (electron LLs) and $n < 0$ (hole LLs) separately form a straight line and converge at $B_\perp = 0$ when extrapolated, within 1 mV, which is our measurement resolution. The slope of each linear-fit line provides the estimation of the v_F value of the corresponding TSS: we obtain $v_F \approx 4.1 \times 10^5$ m s^{-1} for $n < 0$ LLs (red line) and 5.6×10^5 m s^{-1} for $n > 0$ LLs (blue line), and the corresponding bands are assigned to the valence and conduction bands of TSSs in Sb_2Te_3, respectively.

There are, however, two exceptional datasets that do not fall into the LL schemes discussed above. First, the peak of the oscillation corresponding to $n = 0$, started at $V_0 \approx 135$ mV at zero magnetic field, exhibits weak linear dispersion as $B_\perp$ increases, with an estimated g-factor of ~29. Applying an external magnetic field to the TSS breaks the time-reversal symmetry to open a gap, causing a Zeeman energy shift, most greatly affecting the zeroth LL[44]. The experimentally measured g-factors, however, vary widely among the experiments[43–45]. Second, there exists another copy of $n = 0$ and $n = 1$ LL peaks, marked as 0′ and 1′, respectively, emerging at lower bias voltages with smaller intensities. Although their origin is unclear, these modulations do not split from or merge with the main LL peaks.

We now turn our attention to the high bias oscillations (3) discussed above. We identify their peak positions V_n^* and assign the corresponding LL indices (Extended Data Fig. 9), marked by the magenta font (Fig. 4b, top). We then perform a similar analysis as that done for (2) and obtain the corresponding LL origin $V_0^* \approx 647$ mV and velocity $v \approx 1.1 \times 10^6$ m s^{-1} (Fig. 4f, magenta line). In this higher-bias-voltage regime, both E_F^{BS} and E_F^{ST} are outside the BVB and BCB of the counterpart, respectively, and resonant tunnelling can occur between the LLs developed in the TSSs of Bi_2Se_3 and Sb_2Te_3 (see the schematic in Fig. 4f (top inset)). In order for such tunnelling to happen, the quantized energy E_n, angular momentum of LLs ($k_n = \sqrt{2e|n|B_\perp/\hbar}$) and spin–momentum locking helicity of TSSs should be matched. Considering the fact that the two TSSs at the tunnelling interface have opposite spin–momentum locking helicity due to their opposite surface normal directions[46], the only allowed inter-LL resonant tunnelling is the inter-band tunnelling between an occupied $-n$th LL of Bi_2Se_3 to an unoccupied nth LL of Sb_2Te_3, satisfying $eV_n^* + E_D^{BS} - \mathrm{sgn}(n)\, v_F^{BS}\sqrt{2e\hbar|n|B_\perp} = E_D^{ST} + \mathrm{sgn}(n) v_F^{ST}\sqrt{2e\hbar|n|B_\perp}$, where $v_F^{BS(ST)}$ and $E_D^{BS(ST)}$ are the Fermi velocity and Dirac-point energy of the Bi_2Se_3 (Sb_2Te_3) TSS measured with respect to $E_F^{BS(ST)}$, respectively. This relationship results in a straight line in the plot of eV_n^* versus $\mathrm{sgn}(n)\sqrt{|n|B_\perp}$ (Fig. 4f, top), where the slope of this line corresponds to $v_F^{BS} + v_F^{ST}$, which is approximately twice as high as v_F for TSSs of Bi_2Se_3 and those of Sb_2Te_3 (refs. 32,34,41,43,47). This is in agreement with our observation. Thus, the energy–momentum–spin resonance between the two sets of LLs manifests as the sum of the v_F values of the surface states of Bi_2Se_3 and Sb_2Te_3.

Finally, we discuss the effect of $B_\parallel$ on the resonant tunnelling between LLs. As shown in Fig. 4c,d, the ΔG peaks corresponding to inter-LL tunnelling (3) are rapidly suppressed with increasing $B_\parallel$ (for example, compare the LL peaks in the region highlighted by the white dashed box in Fig. 4c with the corresponding $B_\perp$ and V ranges in Fig. 4b,d). The application of $B_\parallel$ leads to an in-plane momentum shift of the tunnelling electrons[6,8,48], which suppresses the inter-band inter-LL resonant tunnelling, where the energy, angular momentum and spin of the electrons must be conserved. Note that the tunnelling from the bulk band to the surface-state LLs (2) is not suppressed by the presence of finite $B_\parallel$ (Fig. 4b–d), since the electron momentum is not quantized in the BCB of Bi_2Se_3 from which the electrons tunnel.

The realization of two different types of TI material epitaxially coupled via an ultrathin crystalline barrier, with atomically sharp and clean interfaces and without chemical intermixing, has allowed us to systematically investigate the selection rules of electron tunnelling between the TSSs. Our results show that the two TSSs can be brought together to a subnanometre distance, which is much shorter than the thickness limit of a single 3D TI slab owing to the wide bandgap of hBN[33,34,49,50]. This system can serve as a platform to explore interesting physics involving coupled TSSs, such as the proposed topological exciton condensation[14,15]. The double-sided vdW epitaxial growth technique can be further applied to various combinations of vdW materials including superconductors and ferromagnets, potentially leading to emergent phenomena and device applications.

Online content

Any methods, additional references, Nature Portfolio reporting summaries, source data, extended data, supplementary information, acknowledgements, peer review information; details of author contributions and competing interests; and statements of data and code availability are available at https://doi.org/10.1038/s41563-024-02079-5.

References

1. Geim, A. K. & Grigorieva, I. V. Van der Waals heterostructures. *Nature* **499**, 419–425 (2013).
2. Novoselov, K. S., Mishchenko, A., Carvalho, A. & Castro Neto, A. H. 2D materials and van der Waals heterostructures. *Science* **353**, aac9439 (2016).
3. Bretheau, L. et al. Tunnelling spectroscopy of Andreev states in graphene. *Nat. Phys.* **13**, 756–760 (2017).
4. Jung, S. et al. Direct probing of the electronic structures of single-layer and bilayer graphene with a hexagonal boron nitride tunneling barrier. *Nano Lett.* **17**, 206–213 (2017).
5. Song, T. et al. Giant tunneling magnetoresistance in spin-filter van der Waals heterostructures. *Science* **360**, 1214–1218 (2018).
6. Mishchenko, A. et al. Twist-controlled resonant tunnelling in graphene/boron nitride/graphene heterostructures. *Nat. Nanotechnol.* **9**, 808–813 (2014).
7. Greenaway, M. T. et al. Resonant tunnelling between the chiral Landau states of twisted graphene lattices. *Nat. Phys.* **11**, 1057–1062 (2015).
8. Wallbank, J. R. et al. Tuning the valley and chiral quantum state of Dirac electrons in van der Waals heterostructures. *Science* **353**, 575–579 (2016).
9. Heremans, J. P., Cava, R. J. & Samarth, N. Tetradymites as thermoelectrics and topological insulators. *Nat. Rev. Mater.* **2**, 17049 (2017).
10. Shibayev, P. P. et al. Engineering topological superlattices and phase diagrams. *Nano Lett.* **19**, 716–721 (2019).
11. Zhao, Y.-F. et al. Tuning the Chern number in quantum anomalous Hall insulators. *Nature* **588**, 419–423 (2020).
12. Deng, P. et al. Topological surface state annihilation and creation in SnTe/$Cr_x(BiSb)_{2-x}Te_3$ heterostructures. *Nano Lett.* **22**, 5735–5741 (2022).
13. Kou, L. et al. Graphene-based topological insulator with an intrinsic bulk band gap above room temperature. *Nano Lett.* **13**, 6251–6255 (2013).
14. Seradjeh, B., Moore, J. E. & Franz, M. Exciton condensation and charge fractionalization in a topological Insulator film. *Phys. Rev. Lett.* **103**, 066402 (2009).
15. Wang, Z., Hao, N., Fu, Z.-G. & Zhang, P. Excitonic condensation for the surface states of topological insulator bilayers. *New J. Phys.* **14**, 063010 (2012).
16. Wang, Z. Y. et al. Superlattices of Bi_2Se_3/In_2Se_3: growth characteristics and structural properties. *Appl. Phys. Lett.* **99**, 023112 (2011).

17. Kim, Y. et al. Remote epitaxy through graphene enables two-dimensional material-based layer transfer. *Nature* **544**, 340–343 (2017).
18. Kong, W. et al. Polarity governs atomic interaction through two-dimensional materials. *Nat. Mater.* **17**, 999–1004 (2018).
19. Hong, Y. J. et al. Van der Waals epitaxial double heterostructure: InAs/single-layer graphene/InAs. *Adv. Mater.* **25**, 6847–6853 (2013).
20. Tchoe, Y. et al. Vertical monolithic integration of wide- and narrow-bandgap semiconductor nanostructures on graphene films. *NPG Asia Mater.* **13**, 33 (2021).
21. Tsen, A. W. et al. Tailoring electrical transport across grain boundaries in polycrystalline graphene. *Science* **336**, 1143–1146 (2012).
22. Park, J. Y. et al. Molecular beam epitaxial growth and electronic transport properties of high quality topological insulator Bi_2Se_3 thin films on hexagonal boron nitride. *2D Mater.* **3**, 035029 (2016).
23. Lapano, J. et al. van der Waals epitaxy growth of Bi_2Se_3 on a freestanding monolayer graphene membrane: implications for layered materials and heterostructures. *ACS Appl. Nano Mater.* **4**, 7607–7613 (2021).
24. Ko, K. et al. Operando electron microscopy investigation of polar domain dynamics in twisted van der Waals homobilayers. *Nat. Mater.* **22**, 992–998 (2023).
25. Liu, Y. et al. Tuning Dirac states by strain in the topological insulator Bi_2Se_3. *Nat. Phys.* **10**, 294–299 (2014).
26. Park, J. Y. et al. Bi_2Se_3 thin films heteroepitaxially grown on α–$RuCl_3$. *Phys. Rev. Mater.* **4**, 113404 (2020).
27. Guha, P. et al. Molecular beam epitaxial growth of Sb_2Te_3–Bi_2Te_3 lateral heterostructures. *2D Mater.* **9**, 025006 (2022).
28. Nakajima, S. The crystal structure of $Bi_2Te_{3-x}Se_x$. *J. Phys. Chem. Solids* **24**, 479–485 (1963).
29. Anderson, T. L. & Krause, H. B. Refinement of the Sb_2Te_3 and Sb_2Te_2Se structures and their relationship to nonstoichiometric $Sb_2Te_{3-y}Se_y$ compounds. *Acta Cryst.* **B30**, 1307–1310 (1974).
30. Takane, D. et al. Work function of bulk-insulating topological insulator $Bi_{2-x}Sb_xTe_{3-y}Se_y$. *Appl. Phys. Lett.* **109**, 091601 (2016).
31. Levy, I. et al. Designer topological insulator with enhanced gap and suppressed bulk conduction in Bi_2Se_3/Sb_2Te_3 ultrashort-period superlattices. *Nano Lett.* **20**, 3420–3426 (2020).
32. Zhang, J. et al. Band structure engineering in $(Bi_{1-x}Sb_x)_2Te_3$ ternary topological insulators. *Nat. Commun.* **2**, 574 (2011).
33. Zhang, Y. et al. Crossover of the three-dimensional topological insulator Bi_2Se_3 to the two-dimensional limit. *Nat. Phys.* **6**, 584–588 (2010).
34. Jiang, Y. et al. Landau quantization and the thickness limit of topological insulator thin films of Sb_2Te_3. *Phys. Rev. Lett.* **108**, 016401 (2012).
35. Yan, R. et al. Esaki diodes in van der Waals heterojunctions with broken-gap energy band alignment. *Nano Lett.* **15**, 5791–5798 (2015).
36. Britnell, L. et al. Electron tunneling through ultrathin boron nitride crystalline barriers. *Nano Lett.* **12**, 1707–1710 (2012).
37. Chandni, U., Watanabe, K., Taniguchi, T. & Eisenstein, J. P. Evidence for defect-mediated tunneling in hexagonal boron nitride-based junctions. *Nano Lett.* **15**, 7329–7333 (2015).
38. Cappelluti, E., Grimaldi, C. & Marsiglio, F. Topological change of the Fermi surface in low-density Rashba gases: application to superconductivity. *Phys. Rev. Lett.* **98**, 167002 (2007).
39. Sun, Y. J. et al. Van Hove singularities as a result of quantum confinement: the origin of intriguing physical properties in Pb thin films. *Nano Res.* **3**, 800–806 (2010).
40. Bahramy, M. S. et al. Emergent quantum confinement at topological insulator surfaces. *Nat. Commun.* **3**, 1159 (2012).
41. Cheng, P. et al. Landau quantization of topological surface states in Bi_2Se_3. *Phys. Rev. Lett.* **105**, 076801 (2010).
42. Hanaguri, T., Igarashi, K., Kawamura, M., Takagi, H. & Sasagawa, T. Momentum-resolved Landau-level spectroscopy of Dirac surface state in Bi_2Se_3. *Phys. Rev. B* **82**, 081305 (2010).
43. Yoshimi, R. et al. Dirac electron states formed at the heterointerface between a topological insulator and a conventional semiconductor. *Nat. Mater.* **13**, 253–257 (2014).
44. Fu, Y.-S. et al. Observation of Zeeman effect in topological surface state with distinct material dependence. *Nat. Commun.* **7**, 10829 (2016).
45. Zhang, Z. et al. Zeeman effect of the topological surface states revealed by quantum oscillations up to 91 Tesla. *Phys. Rev. B* **92**, 235402 (2015).
46. Fluckey, S. P., Tiwari, S., Hinkle, C. L. & Vandenberghe, W. G. Three-dimensional-topological-insulator tunnel diodes. *Phys. Rev. Appl.* **18**, 064037 (2022).
47. Xia, Y. et al. Observation of a large-gap topological-insulator class with a single Dirac cone on the surface. *Nat. Phys.* **5**, 398–402 (2009).
48. Wang, L.-X. et al. Zeeman effect on surface electron transport in topological insulator Bi_2Se_3 nanoribbons. *Nanoscale* **7**, 16687–16694 (2015).
49. Jin, H., Im, J., Song, J.-H. & Freeman, A. J. Multiple Dirac fermions from a topological insulator and graphene superlattice. *Phys. Rev. B* **85**, 045307 (2012).
50. Costa, M. et al. Controlling topological states in topological/normal insulator heterostructures. *ACS Omega* **3**, 15900–15906 (2018).

Publisher's note Springer Nature remains neutral with regard to jurisdictional claims in published maps and institutional affiliations.

Springer Nature or its licensor (e.g. a society or other partner) holds exclusive rights to this article under a publishing agreement with the author(s) or other rightsholder(s); author self-archiving of the accepted manuscript version of this article is solely governed by the terms of such publishing agreement and applicable law.

© The Author(s), under exclusive licence to Springer Nature Limited 2025

[1]Department of Physics, Harvard University, Cambridge, MA, USA. [2]Department of Physics and Astronomy, and Institute of Applied Physics, Seoul National University, Seoul, Republic of Korea. [3]Department of Materials Science and Engineering, and Research Institute of Advanced Materials, Seoul National University, Seoul, Republic of Korea. [4]Department of Physics, Sogang University, Seoul, Republic of Korea. [5]Center for Nanoscale Systems, Harvard University, Cambridge, MA, USA. [6]Department of Energy Engineering, Ulsan National Institute of Science and Technology (UNIST), Ulsan, Republic of Korea. [7]Department of Physics, Florida State University, Tallahassee, FL, USA. [8]National High Magnetic Field Laboratory, Florida State University, Tallahassee, FL, USA. [9]Research Center for Electronic and Optical Materials, National Institute for Materials Science, Tsukuba, Japan. [10]Research Center for Materials Nanoarchitectonics, National Institute for Materials Science, Tsukuba, Japan. [11]Department of Energy and Department of Chemistry, Sungkyunkwan University (SKKU), Suwon, Republic of Korea. [12]Center for 2D Quantum Heterostructures, Institute for Basic Science (IBS), Sungkyunkwan University (SKKU), Suwon, Republic of Korea. ✉e-mail: gcyi@snu.ac.kr; pkim@physics.harvard.edu

Methods

Preparation of suspended ultrathin hBN and graphene

For vertical tunnel junctions, atomically thin hBN single-crystal flakes are prepared by mechanical exfoliation on the oxygen-plasma-treated surfaces of Si substrates with a 90 nm SiO_2 layer and identified by optical microscopy. The thickness and surface cleanliness of the identified layers are further characterized by atomic force microscopy. We choose 2–5 ML hBN for the tunnel barrier because they provide reliably working tunnel junctions over a suitable current and bias-voltage range. The target flake is then picked up and transferred onto perforated SiN_x membranes using sticky polymer films, such as polycaprolactone[51] or polycarbonate, on polydimethylsiloxane stamps. Here we use 50-nm-thick low-stress silicon-rich nitride membranes with TEM-compatible silicon frames (Silson). Arrays of holes with typical diameters of 0.4–1 μm are fabricated in the SiN_x membranes by standard electron-beam (e-beam) lithography and CF_4/Ar reactive ion etching. The oxygen plasma treatment of the SiN_x membranes immediately before the drop-down process enhances the adhesion between the vdW layers and the membranes, reducing the risk of washing away of the flake or wrinkle formation during the subsequent wet process. After the transfer, the sticky polymer is removed by organic solvents: tetrahydrofuran for polycaprolactone and chloroform for polycarbonate. Finally, the sample is annealed (typically at 350–400 °C) under a high vacuum to reduce the polymer residues. For plan-view TEM study of the double-sided vdW epitaxial heterostructures, we also use few-layer hBN epitaxially grown on a sapphire substrate[52] and monolayer graphene grown on a Cu foil. These chemical-vapour-deposition-grown large-scale vdW substrate layers are suspended on holey SiN_x membranes by the poly(methyl methacrylate)-assisted wet transfer method. The suspended vdW layer undergoes another round of in situ thermal cleaning in the UHV MBE chamber before the growth of TI thin films.

Double-sided vdW MBE growth

First, unless otherwise stated, Bi_2Se_3 thin films are typically grown first on the bottom surface of suspended hBN or graphene through the holes in the SiN_x membranes by loading the chip upside down on a substrate holder of the MBE. We use the two-step growth process developed for high-quality Bi_2Se_3 thin-film growth on vdW layered substrates[22,26]. The top surface of the suspended vdW layer remains intact after bottom-side growth, preserving its atomically clean surface (Fig. 1h). This growth result is attributed to the highly directional molecular fluxes of the precursors, which are hardly subject to scattering events during MBE growth in a UHV environment. Next, the substrate is inverted ex situ and loaded back into the MBE chamber so that the top side faces the molecular fluxes. Another round of two-step MBE growth is then performed to grow either Bi_2Se_3 or Sb_2Te_3 thin films on top of the hBN (graphene)/Bi_2Se_3 heterostructure using a similar two-step growth process[27]. In this step, care is taken to protect the pre-grown Bi_2Se_3 such as omitting the thermal cleaning process and reducing the second-step growth temperature. The bottom TI film has crystalline structures up to the interface with hBN and exhibits similar structural quality to the top TI film (Fig. 2b,f and Extended Data Fig. 3), indicating that the hBN layer effectively protects the bottom TI–hBN interface from the environment during the ex situ sample flipping and subsequent growth of the top layer. The typical thickness of the TI films is 20 QL for the top side and 10 QL for the bottom side (Extended Data Fig. 2). Further advancements in the process, such as in situ flipping, selective area growth and simultaneous double-sided growth, could improve the quality of the double-sided heterostructure and enhance the applicability of this method.

Microstructural characterizations

The plan-view TEM study is conducted directly on the as-grown samples without any post-growth processes. This is possible because the suspended vdW heterostructures are electron transmitting, and our SiN_x membrane chips are TEM compatible. Field-emission TEMs with an acceleration voltage of 200 kV (JEOL JEM-2100F and FEI Tecnai F20) are used for HR imaging and SAED measurements. An average background subtraction filter is applied to remove noise in the HR-TEM images. The TEM lamella for the cross-sectional study is prepared by a focused ion beam system (FEI Helios 650). The elemental distribution mapping is performed with a silicon-drift-detector-based energy-dispersive X-ray spectroscopy system operating in the scanning TEM mode and analysed with AZtec TEM software (Oxford Instruments).

Device fabrication

Electrical contacts on both sides of the suspended TI/hBN/TI heterostructures, prepared on SiN_x membrane templates, are fabricated by the following steps. First, a Ti/Au (5/200 nm) metal layer is deposited on the bottom side of the sample by e-beam evaporation. The thick metal layer provides ohmic contacts to the bottom TI and mechanical support to the membrane for the subsequent fabrication steps. Note that the frames of our membrane chips are made of high-resistivity silicon, which becomes insulating at low temperatures. The individual top ohmic contacts to the array of junctions are fabricated by e-beam lithography followed by the e-beam evaporation of Ti/Au (5/55 nm). Using the metal contacts as etch masks, Ar plasma etching is carried out to remove the TI films on the uncovered area, electrically separating the array of junctions. Finally, bonding pads and interconnection lines to the contacts are deposited by another round of e-beam lithography and e-beam evaporation of Ti/Pd/Au (5/20/125 nm). Considering the lateral diffusion growth of the TI film between the SiN_x membrane and hBN layer, the nominal junction area defined by the size of the holes in the SiN_x membrane is in the range of 0.2–0.7 μm^2.

Magneto-tunnelling measurements

The current–voltage characteristics of the tunnelling devices are measured using a voltage source (Yokogawa GS200 d.c. voltage source or Keithley Instruments 2400 source meter) to apply a d.c. bias voltage and a low-noise current preamplifier (DL Instruments Model 1211) connected to a digital multimeter (Agilent 34401A) for measuring the current. The differential conductance is measured simultaneously with the current–voltage curve by mixing the d.c. bias voltage with a small a.c. excitation voltage of 1 mV at 47.77 Hz using a lock-in amplifier (Stanford Research Systems SR830), a voltage divider and a transformer. Temperature and magnetic field are controlled by ^{4}He variable-temperature inserts equipped with superconducting magnets (Physical Property Measurement System (Quantum Design), TeslatronPT (Oxford Instruments) and DStat (Cryo Industries of America)). The angle of the magnetic fields with respect to the tunnelling interface is controlled by changing the orientation of the sample ex situ. For each field angle, tunnelling characteristics at zero magnetic field are cross-checked to confirm the robustness of the tunnelling conductance against thermal cycling. The Bi_2Se_3/hBN/Bi_2Se_3 device presented in Extended Data Fig. 6 is measured using a ^{3}He cryostat with a 31.5 T resistive magnet at the National High Magnetic Field Laboratory. A rotator probe is used to change the sample orientation in situ. During the device fabrication, loading and shipping processes, meticulous measurements are implemented to prevent electrostatic discharge.

Data availability

The data that support the findings of this study are presented in the Article and its Extended Data. Further data are available from the corresponding authors upon reasonable request.

References

51. Son, S. et al. Strongly adhesive dry transfer technique for van der Waals heterostructure. *2D Mater.* **7**, 041005 (2020).
52. Jang, A. R. et al. Wafer-scale and wrinkle-free epitaxial growth of single-orientated multilayer hexagonal boron nitride on sapphire. *Nano Lett.* **16**, 3360–3366 (2016).

Acknowledgements
We thank J. Eom, Y. S. Kim and C.-H. Lee for their assistance with transferring atomically thin vdW crystals onto perforated SiN_x membranes. We also express our gratitude to S. Cho and Effucell for providing technical support with the UHV MBE system. Additionally, we thank J. S. Lee of the National Center for Inter-University Research Facilities at Seoul National University for assistance with the focused ion beam system. The major part of this work was supported by the Office of Naval Research (ONR) Multidisciplinary University Research Initiatives (MURI) program (N00014-21-1-2377) and the Science Research Center (SRC) for Novel Epitaxial Quantum Architectures (NRF-2021R1A5A1032996). J.Y.P. and P.K. acknowledge support from ONR (N00014-24-1-2081). J.S., J.K. and D.K. acknowledge support from the National Research Foundation of Korea (NRF) grants funded by the Korean Government (grant nos. RS-2023-00283291, RS-2023-00207732 and 2023R1A2C2005809). J.J. and M.K. acknowledge support from the NRF (NRF-2022R1A2C3007807). H.Y. acknowledges support from the NRF (grant nos. 2021R1C1C1010924 and 2020R1F1A1049563). H.S.S. acknowledges support from the Institute for Basic Science (IBS-R036-D1). A portion of the user collaboration grant program (UCGP) project was performed at the National High Magnetic Field Laboratory supported by the National Science Foundation through NSF/DMR-1644779 and the State of Florida. K.W. and T.T. acknowledge support from the JSPS KAKENHI (grant nos. 20H00354 and 23H02052) and World Premier International Research Center Initiative (WPI), MEXT, Japan.

Author contributions
P.K., G.-C.Y. and J.Y.P. conceived the experiments. J.Y.P. performed the double-sided vdW epitaxy and fabricated the tunnelling devices. J.Y.P. and G.-C.Y. analysed and optimized these processes. J.Y.P. performed the magneto-tunnelling measurements together with J.S. and J.K. J.Y.P., R.M.H., A.G. and W.K.P. carried out the measurements at the National High Magnetic Field Laboratory. J.Y.P., J.S., J.K., D.K. and P.K. analysed the transport data. J.J. conducted the TEM experiments. J.J., J.Y.P., G.-C.Y. and M.K. analysed the TEM data. J.Y.P. and H.Y. prepared the hole-patterned SiN_x membrane templates. Y.J.S., D.H., H.Y. and J.Y.P. carried out the suspension of ultrathin vdW layers on the perforated SiN_x membranes. C.H. and H.S.S. provided the epitaxial few-layer hBN films and collaborated on discussions about the double-sided vdW epitaxy on them. J.Y. grew the monolayer graphene. K.W. and T.T. provided the bulk hBN single crystals. G.-C.Y. and P.K. jointly supervised the project. J.Y.P. and P.K. wrote the manuscript with input from all authors.

Competing interests
The authors declare no competing interests.

Additional information
Extended data is available for this paper at https://doi.org/10.1038/s41563-024-02079-5.

Correspondence and requests for materials should be addressed to Gyu-Chul Yi or Philip Kim.

Peer review information *Nature Materials* thanks Xiangfeng Duan and the other, anonymous, reviewer(s) for their contribution to the peer review of this work.

Reprints and permissions information is available at www.nature.com/reprints.

https://doi.org/10.1038/s41563-024-02079-5

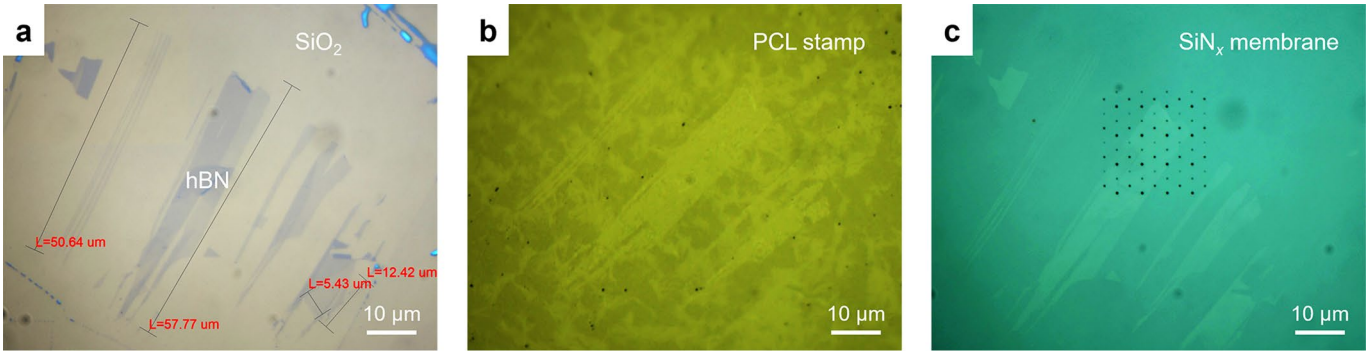

Extended Data Fig. 1 | Suspension of atomically thin hBN crystals on the perforated SiN_x membrane. a–c, Optical microscope images of ultrathin hBN layers: as exfoliated on the SiO_2 surface (**a**), picked up by the PCL polymer stamp (**b**), transferred on the SiN_x membrane with premade holes (**c**).

https://doi.org/10.1038/s41563-024-02079-5

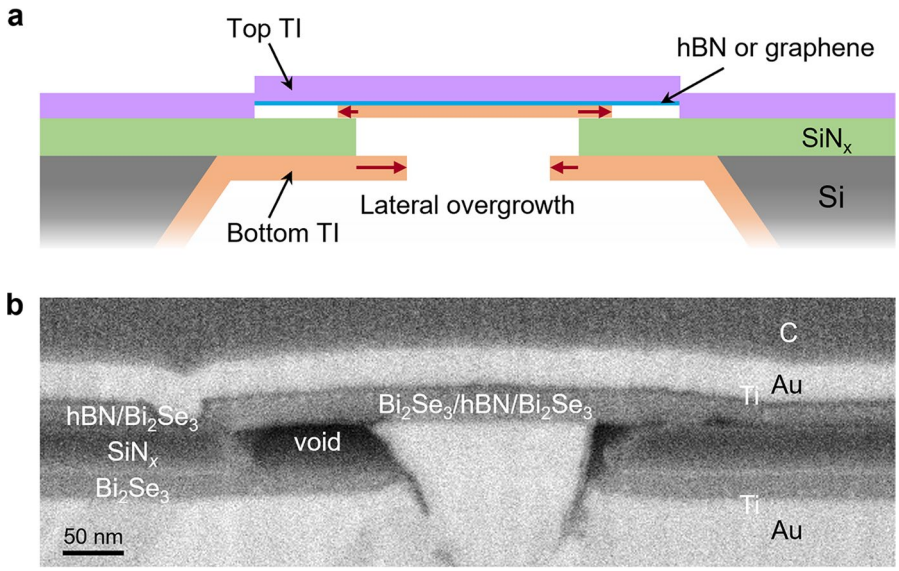

Extended Data Fig. 2 | Lateral overgrowth of the bottom TI layer. Cross-sectional schematic illustration (**a**; not drawn to scale) and scanning electron microscopy image (**b**; 52° tilted view) of the sample shown in Fig. 3a, depicting the lateral overgrowth of the bottom TI layer at the hBN(graphene)/SiN_x interface and the bottom edge of the hole in the SiN_x membrane. This is due to lateral diffusion of adatoms at the vdW terminated growth front, resulting in highly anisotropic growth that favors lateral over vertical growth. The growth rate is slower at the bottom of the suspended vdW layer due to the shadowing effect of the TI films laterally grown over the bottom edge of the hole in the SiN_x.

https://doi.org/10.1038/s41563-024-02079-5

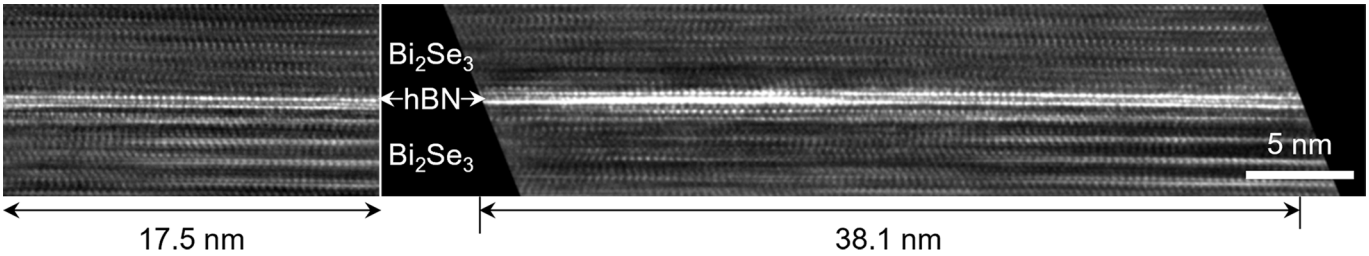

Extended Data Fig. 3 | Larger scale homogeneity of the Bi_2Se_3/hBN/Bi_2Se_3 interface. Cross-sectional HR-TEM images of Bi_2Se_3/2 ML hBN/Bi_2Se_3 taken along the zone axis $[1\bar{2}10]$ exhibiting atomically sharp and clean interfaces.

https://doi.org/10.1038/s41563-024-02079-5

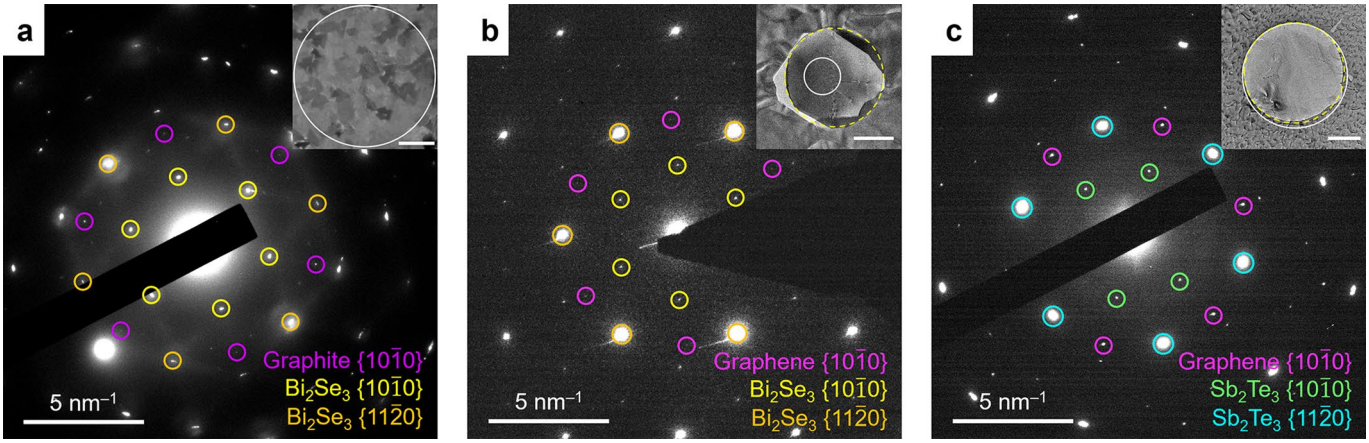

Extended Data Fig. 4 | Epitaxial relationship of the TI thin films grown on a single surface of suspended graphene substrates. a–**c**, Plan-view SAED patterns of the Bi_2Se_3 thin film grown on the top surface of suspended graphite (**a**), the Bi_2Se_3 thin film grown on the bottom surface of suspended monolayer graphene (**b**), and the Sb_2Te_3 thin film grown on the top surface of suspended monolayer graphene (**c**). Insets: Plan-view TEM BF images. The white solid circles and the yellow dashed circles indicate the areas in which the SAED in the corresponding main panels are taken and the suspended regions, respectively. The entire area displayed in the inset is suspended for **a**. Scale bars in the insets: 1 µm (**a**), 200 nm (**b**), and 200 nm (**c**). All data (**a**–**c**) exhibit the preferential epitaxial relationship of $\{10\bar{1}0\}_{Bi_2Se_3 \text{ or } Sb_2Te_3} \parallel \{10\bar{1}0\}_{\text{graphene or graphite}}$, indicating that the epitaxial alignment in the double-sided vdW epitaxy is owing to the local interaction at the interface with the suspended vdW substrate layer.

https://doi.org/10.1038/s41563-024-02079-5

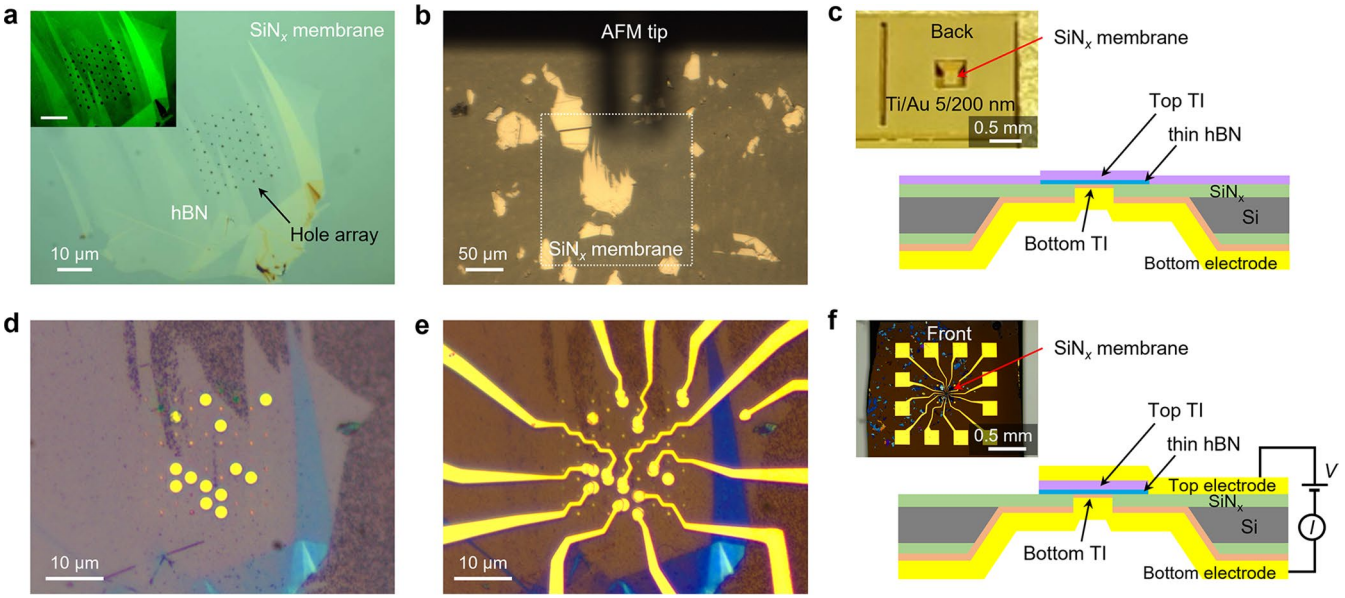

Extended Data Fig. 5 | Tunneling device fabrication processes. a, Optical microscope image of atomically thin hBN layers suspended on the perforated SiN_x membrane. Inset: High-contrast image of the main panel. Scale bar: 10 µm. **b**, Optical microscope image of the sample in (**a**) after the double-sided vdW epitaxy of TI thin films (10 QL Bi_2Se_3 on the back side and 20 QL Sb_2Te_3 on the top side). **c**, Photograph (upper left) and schematic (lower right) of the double-sided vdW epitaxial heterojunction after the evaporation of the Ti/Au 5/200 nm common bottom contact. **d**,**e**, Optical microscope images of the junction arrays: after the fabrication of Ti/Au 5/55 nm individual top contacts followed by Ar plasma etching (**d**) and after the formation of bonding pads and leads (Ti/Pd/Au 5/20/125 nm). **f**, Optical microscope image (upper left) and schematic structure (lower right) of the finished device.

https://doi.org/10.1038/s41563-024-02079-5

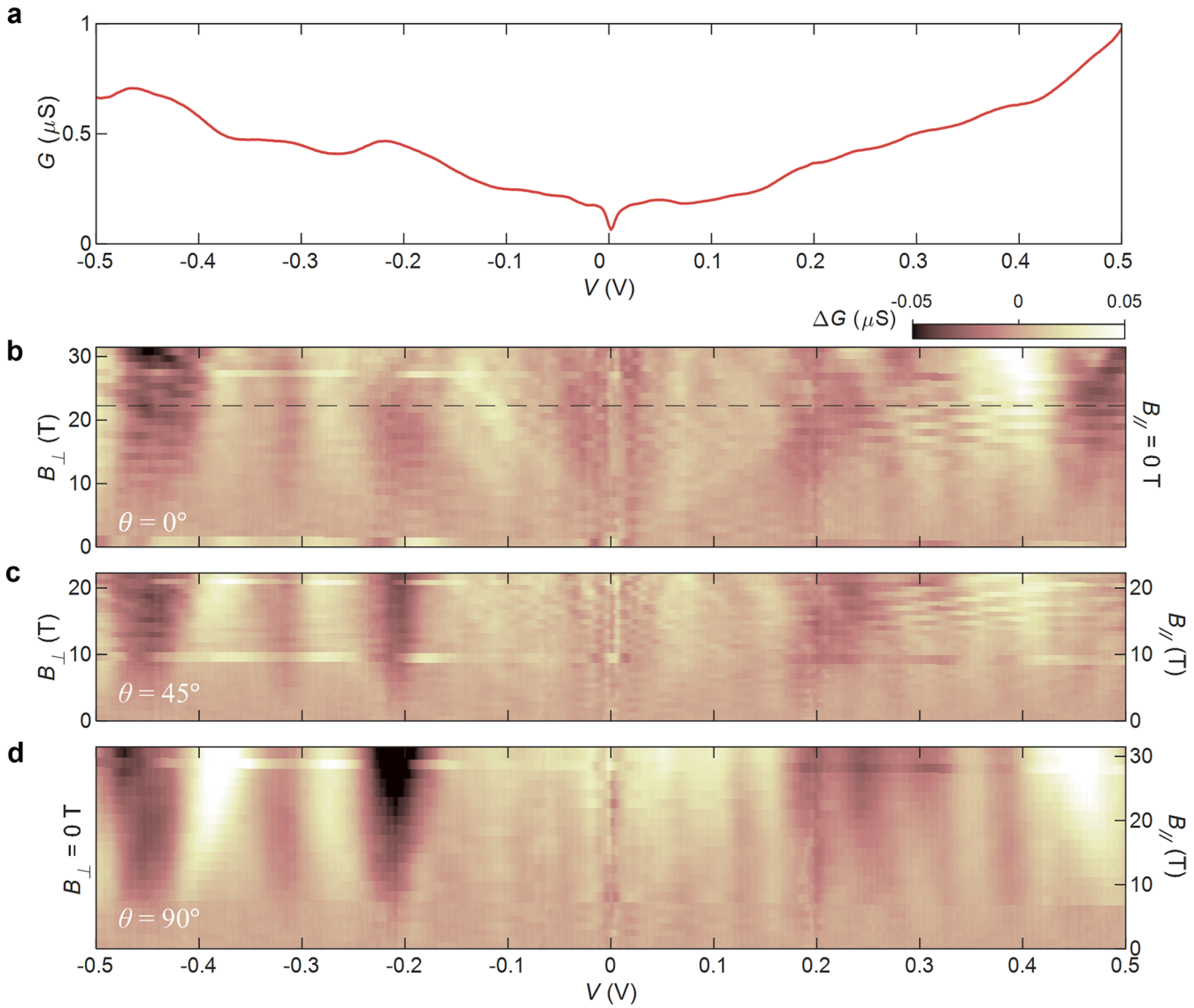

Extended Data Fig. 6 | Magnetic field-dependent tunnelling conductance of a Bi_2Se_3/3 ML hBN/Bi_2Se_3 device. a, Differential conductance $G(V) = \partial I/\partial V$ of the Bi_2Se_3/3 ML hBN/Bi_2Se_3 device at zero magnetic field. **b**–**d**, Colour scale maps showing the field-modulated component of the conductance $\Delta G(V, B)$ at different field angles: out-of-plane (**b**), 45° tilted (**c**), and in-plane (**d**) directions. $B_\perp$ and $B_\parallel$ components of the field are indicated by the left and right ticks, respectively. The black dashed horizontal line in **b** indicates the maximum $B_\perp$ in **c**. We observe oscillatory features that develop at higher $B_\perp$, with their peak and valley positions varying as a function of $B_\perp$, in addition to the field-angle-independent oscillatory features arising from the bulk QWSs. We are however unable to conclusively identify conductance oscillations associated with the LL formation in TSSs, presumably because the conductance is dominated by the bulk-to-bulk tunnelling as both the b- and t-Bi_2Se_3 films are degenerately n-doped. The difference in thickness between the b-Bi_2Se_3 (10 QL) and t-Bi_2Se_3 (20 QL) is responsible for the asymmetry in the periodicity of the QWS-related oscillations at negative and positive biases. All measurements are performed at $T = 0.3$ K.

https://doi.org/10.1038/s41563-024-02079-5

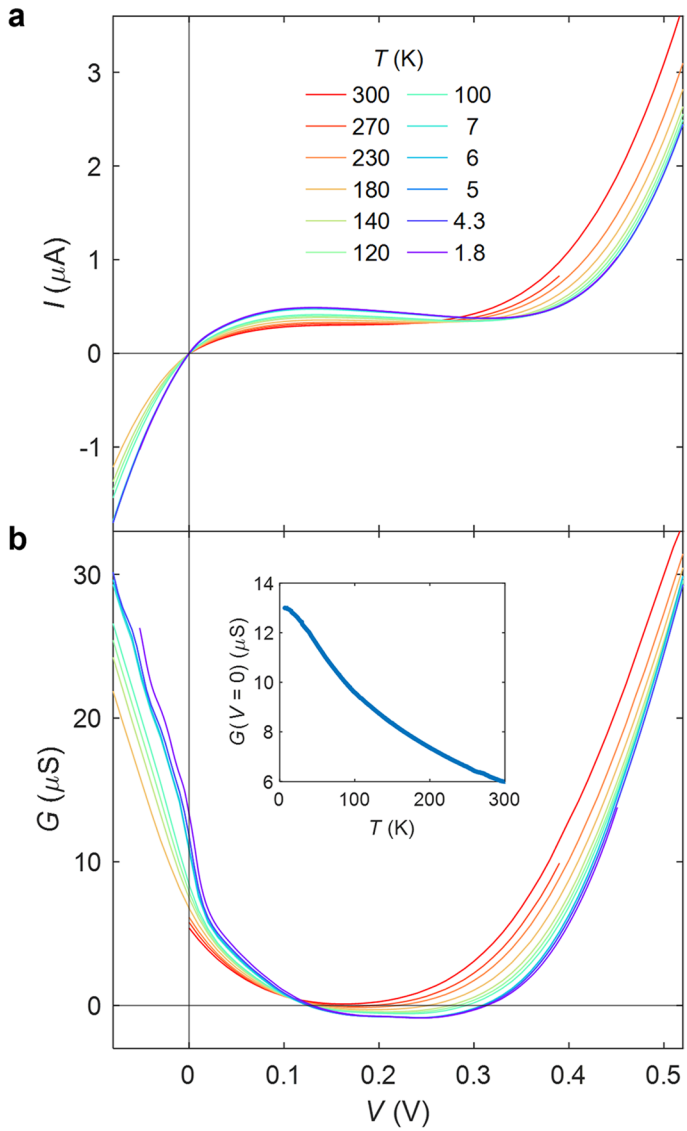

Extended Data Fig. 7 | Temperature dependence of tunnelling current and tunnelling conductance. a,**b**, Tunnelling current $I(V)$ (**a**) and differential conductance $G(V) = \partial I/\partial V$ (**b**) of Bi_2Se_3/3 ML hBN/Sb_2Te_3 device at different temperatures. Inset: Zero-bias differential conductance $G(V = 0)$ as a function of temperature. The NDC behaviour is enhanced as temperature decreases, consistent with the broken-gap energy band alignment picture[35]. The bulk-originated oscillatory features ($V < 0$) and the local maximum in G (V ~0.22 V) become evident at $T \leq 7$ K of our data.

https://doi.org/10.1038/s41563-024-02079-5

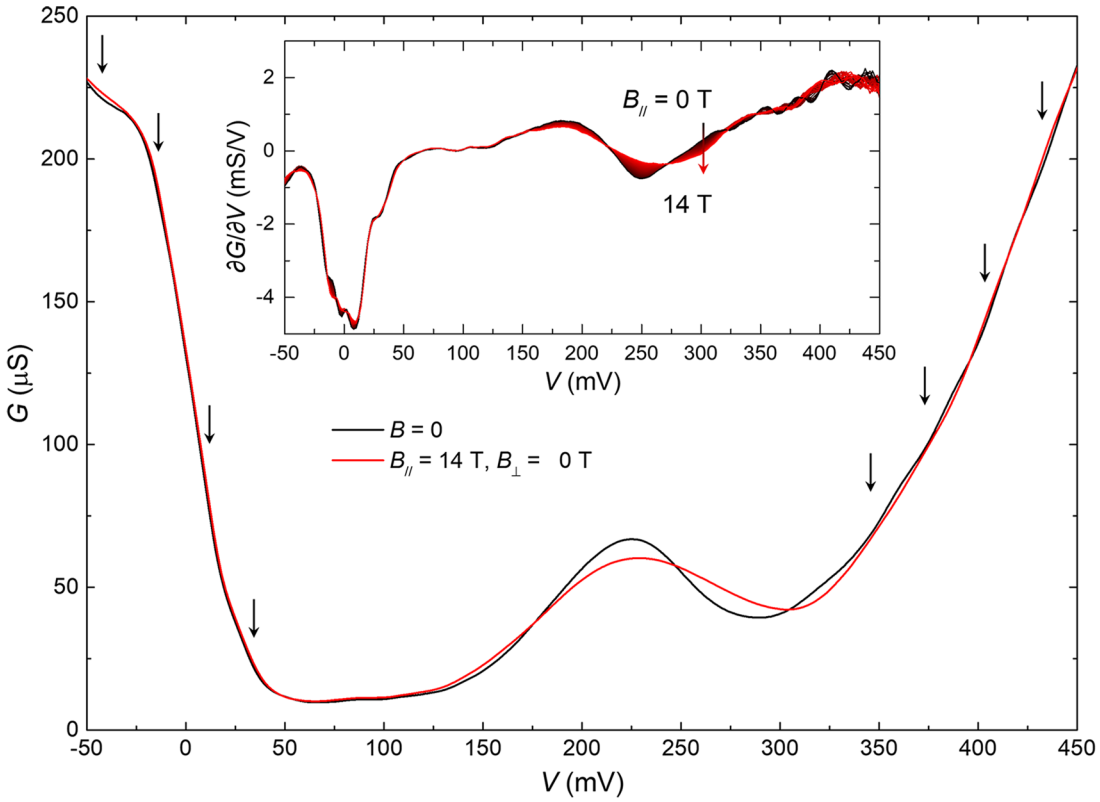

Extended Data Fig. 8 | Oscillations in the tunnelling conductance associated with the bulk QWSs. Differential conductance $G(V) = \partial I/\partial V$ of the Bi_2Se_3/2 ML hBN/Sb_2Te_3 device at zero magnetic field (black) and $B_{\parallel} = 14$ T (red). The inset shows $\partial G/\partial V = \partial^2 I/\partial V^2$ as a function of V at different $B_{\parallel}$, obtained by taking numerical derivative of $G(V)$. The black arrows indicate the positions of the peaks of the oscillatory feature (1) related to the bulk QWSs, appearing in $\Delta G(V, B)$ (Fig. 4b–e). One can find that they correspond to the valleys of the QWS resonances in $G(V, B = 0)$, which become smoothened out at higher $B_{\parallel}$ as fine structures develop due to the Zeeman effects. The $G(V, B = 0)$ peak at $V = 225$ mV, attributed to the alignment of the bulk band edges, is also suppressed at higher $B_{\parallel}$ by the Zeeman effects. All data is measured at $T = 1.8$ K.

https://doi.org/10.1038/s41563-024-02079-5

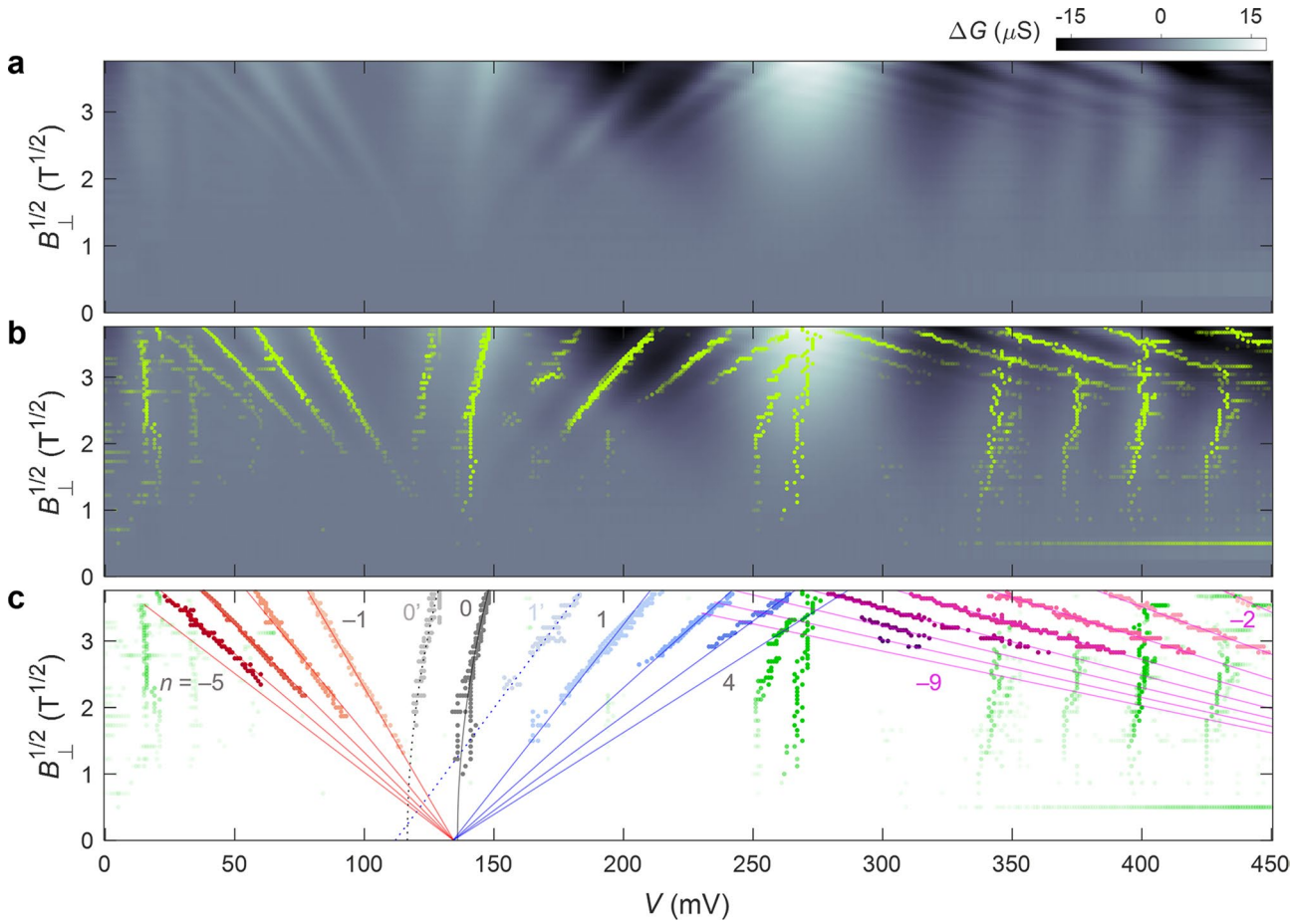

Extended Data Fig. 9 | LL peak identifications and LL index assignments. **a**, Field-modulated component of the tunnelling conductance $\Delta G(V, B)$ at $\theta = 0°$ and $T = 1.8$ K, the same data as Fig. 4b replotted with $B_\perp^{1/2}$ as the vertical axis so that the LLs formed in the Dirac states appear as linear lines, ignoring the Zeeman energy. **b**, Peaks identified in **a**. The lime-coloured dots represent the peak positions identified by MATLAB's *findpeaks* function, a tool for locating local maxima, applied along the vertical and horizontal axes, as well as in two diagonal directions. The transparency of the dots corresponds to the prominence of the peaks the function returns. **c**, LL index assignments. The positions of the peaks assigned to each LL index n are indicated by the corresponding colour. The green dots are the positions of the peaks not associated with the LLs. The solid lines tracing the peaks corresponding to $n < 0$ (red) and $n > 0$ (blue) LLs of Sb_2Te_3, and the inter-band inter-LL resonant tunneling between Bi_2Se_3 and Sb_2Te_3 (magenta) are reconstructed from the slopes and intercepts of the linear fits in Fig. 4f. The dark grey curve is a fit to the $n = 0$ LL peaks shifting linearly with respect to $B_\perp$. The dotted curve and line trace the $n = 0'$ and $1'$ LL peaks of unclear origin, respectively.